aerospace

MDPI

Article

A Star Map Matching Method Based on Magnitude Stratification and Seed Diffusion for Dense Star Scenes

Yasheng Zhang, Jiayu Qiu, Can Xu, Yuqiang Fang and Kaiyuan Zheng *

Graduate School, Space Engineering University, Beijing 101416, China; zhangyspublic@163.com (Y.Z.); qiuuujy@hgd.edu.cn (J.Q.); canxu1985@163.com (C.X.); fangyuqiang@nudt.edu.cn (Y.F.)
* Correspondence: kaiyuan_zheng@hgd.edu.cn

Abstract

Astronomical positioning of space targets is an important task in space situational awareness. In both ground-based and space-based optical observation scenarios, accurate positioning relies on the reliable matching of numerous stars in observational images. However, dense star scenes increase the ambiguity of local patterns and the computational burden of candidate retrieval. Building on established geometric voting and catalog-indexing strategies, this paper develops a two-stage star map matching method that specifically combines adaptive magnitude stratification with seed-guided residual-star diffusion for large-field dense star scenes. In the first stage, an adaptive magnitude-stratified bright-star subset is selected according to field density, and angular-distance voting is used to obtain reliable seed correspondences. In the second stage, residual-star candidates are retrieved from seed-centered dual-feature sub-libraries indexed by angular distance and magnitude difference, and are then refined through single-seed local diffusion and multi-seed global fusion. Experimental results from both simulated and real observational data demonstrate that the proposed method achieves a high matching success rate with low computational cost and performs effectively in large-field, dense star scenes. The proposed method provides a practical matching solution for astronomical positioning in dense star scenes.

Keywords: space situational awareness; star map matching; astronomical positioning of space objects; dense star scenes

1. Introduction

Space situational awareness (SSA) is a core technology for ensuring space security and supporting the orderly conduct of space activities. Among its many monitoring targets, high-orbit space objects have become a major research focus because of their strategic importance and practical value. In this context, large-field-of-view optical detection systems are playing an increasingly important role in high-orbit SSA missions because of their high detection efficiency and superior resolution [1–4]. In addition to ground-based optical surveillance, space-based optical sensors and onboard star trackers are also being explored as opportunistic SSA sensors. For example, star trackers have been used for space-object detection and monitoring [5,6]. These space-based scenarios further highlight the importance of reliable stellar-background identification, because dense stellar fields and simultaneously observed moving objects must be separated before target detection, positioning, and orbit-related analysis. Accordingly, star map matching is no longer merely a routine preprocessing step; rather, it has become a critical enabling technology that directly affects the reliability, timeliness, and level of automation of optical SSA pipelines. Meanwhile,

Academic Editor: Xiaofeng Wu

Received: 21 April 2026
Revised: 11 May 2026
Accepted: 11 May 2026
Published: 13 May 2026

improvements in detector sensitivity and limiting magnitude have dramatically increased the number of stars captured in a single frame, transforming star map matching from a relatively sparse identification problem into a dense-scene correspondence problem with much greater ambiguity and computational complexity.

Star map matching is a fundamental task in astronomical image registration, star-sensor attitude determination, and optical target positioning. Its core objective is to establish reliable correspondences between observed stars and catalog stars so that the celestial reference frame can be accurately transferred to the image plane [7–11]. Groth [12] proposed a classical triangle-based matching algorithm using side-length ratios and angular cosines as invariant features. Padgett [13] developed a grid-based method that improves matching efficiency through exclusive grid patterns and lookup-table retrieval. Building on these pioneering studies, later research mainly focused on improving robustness and efficiency through further algorithmic innovation.

For example, He et al. [14] transformed the matching process from global to local processing based on icosahedral spherical segmentation, thereby improving efficiency. Yuan [15] proposed a global multi-triangle voting algorithm that reduces the dimensionality of angular-distance vectors through principal component analysis (PCA) and discretization, which lowers the computational burden while improving result reliability through global voting. Liu et al. [16] adopted a two-step strategy of central local matching followed by global matching. They first obtained rough plate constants by gradually expanding the central field of view and then improved positioning accuracy through global high-order fitting, while preserving the integrity of the raw data.

To improve robustness under interference, several studies have addressed the problems of false stars and missing stars. Gustavo et al. [17] constructed five-vertex polygon features to reduce misidentification caused by noise. Jiang et al. [18] proposed an identification method based on joint stellar distribution, in which polygon features are built from the intersection points of triangle perpendicular bisectors and represented by multiple geometric parameters. Mehta et al. [19] proposed a rotation-invariant additive vector sequence technique, which effectively handles missing stars and false stars. Kim et al. [20] further introduced singular values and Gaussian mixture models (GMMs) into star map matching by extracting invariant features through singular value decomposition (SVD) and discretizing them. Wei et al. [21] proposed a graph-based star map recognition algorithm based on angular-distance matching score propagation. Zhao et al. [22] introduced a nearest-neighbor distance index to narrow the range of candidate reference stars. Dai et al. [23] proposed a dynamic distance-ratio matching algorithm. Sun et al. [24] proposed a robust and high-accuracy star map matching algorithm for dense star scenes, using a coarse-to-fine two-stage framework based only on inter-star angular features to improve robustness and efficiency under high star density, false stars, and centroid-position errors.

Overall, classical studies mainly relied on geometric invariants such as triangles, grids, radial patterns, and pairwise angular relationships. These methods were effective when the number of stars per frame was limited and the candidate search space remained manageable. In recent years, the field has developed toward richer local descriptors, voting strategies, graph-based propagation, and structured catalog indexing. This shift is closely related to the availability of large and precise stellar catalogs. Gaia Data Release 3 (Gaia DR3), for example, provides more than 1.8 billion sources [25]. However, improved catalog quality also intensifies the practical challenge of matching: increased catalog completeness and deeper imaging sharply raise the number of candidate correspondences and redundant local patterns, and sensitivity to noise or false detections.

To address this challenge, this study builds on established geometric voting and catalog-indexing ideas and develops a task-specific two-stage matching implementation for large-field dense star scenes. The method follows a coarse-to-fine structure, but its emphasis is placed on the coordinated use of three components. First, an adaptive magnitude-stratification strategy is used to select a compact and relatively stable bright-star subset according to the field density, so that the initial matching stage is performed on reliable anchor stars rather than on the full dense catalog. Second, after bright-star correspondences are obtained, a residual-star diffusion feature library is activated around the matched seed stars, where angular distance and magnitude difference are jointly used to constrain candidate retrieval. Third, single-seed local diffusion and multi-seed global fusion are combined to suppress locally plausible but globally inconsistent residual-star matches.

In this sense, the contribution of this work is incremental but practical; it integrates adaptive bright-star stratification, dual-feature residual-star diffusion, and multi-seed fusion into a unified matching workflow for dense star scenes. The effectiveness of this combination is evaluated using simulated datasets with different star densities, positional noise levels, and false-star interference, as well as measured data from a large-field telescope. The remainder of this paper is organized as follows: Section 2 describes the analytical model and algorithmic implementation; Section 3 presents the experimental validation and comparison with representative methods; and Section 4 provides the discussion and conclusions.

2. Materials and Methods

To address the requirements of accuracy, robustness, and efficiency for star map matching in large-field dense star scenarios, this paper proposes a two-stage method based on magnitude stratification and seed diffusion.

In the first stage, an adaptive magnitude-threshold analysis is performed to select a globally stable bright-star subset from the Gaia DR3 catalog, from which a bright-star angular-distance library is constructed for coarse matching. The resulting bright-star correspondences provide reliable seed stars for the second stage. In the second stage, we construct an offline diffusion feature library for residual stars, in which each catalog bright star is associated with a local dual-feature sub-library indexed by quantized angular distance and quantized magnitude difference. During online matching, only the sub-libraries associated with successfully matched seed stars are accessed, thereby avoiding exhaustive retrieval over the full catalog. Residual-star identification is then completed through a two-step strategy of single-seed local diffusion and multi-seed global fusion, in which geometric consistency, photometric consistency, and hierarchical diffusion weights are jointly integrated into the voting process. This design yields a complete pipeline from bright-star coarse matching to residual-star fine matching and provides a scalable solution for astronomical positioning and high-orbit situational awareness. The overall pipeline is illustrated in Figure 1.

The proposed implementation consists of two coordinated stages: magnitude-stratified bright-star anchoring and seed-guided residual-star diffusion. The first stage aims to obtain reliable global anchors from a compact bright-star subset, whereas the second stage uses these anchors to constrain and fuse residual-star candidate matches.

In the first stage, adaptive magnitude-threshold analysis is used to select a compact bright-star subset from Gaia DR3 under the FOV and field-density constraints. A bright-star angular-distance library is then constructed to support coarse voting-based matching, and the validated bright-star correspondences are used as seed stars for the residual-star stage. In the second stage, an offline diffusion feature library is constructed for residual stars, in which each catalog bright star is associated with a local dual-feature sub-library indexed by quantized angular distance and quantized magnitude difference. During online matching, only the sub-libraries corresponding to successfully matched seed stars are accessed, which reduces exhaustive retrieval over the dense catalog. Residual-star identification is then performed within the seed-guided stage by combining single-seed local diffusion with multi-seed global fusion, where geometric consistency, photometric consistency, and hierarchical diffusion weights are jointly integrated into the voting process. This organization is intended to reduce online retrieval redundancy and improve matching stability in dense scenes, while remaining compatible with established angular-distance voting principles. The overall pipeline is illustrated in Figure 1.

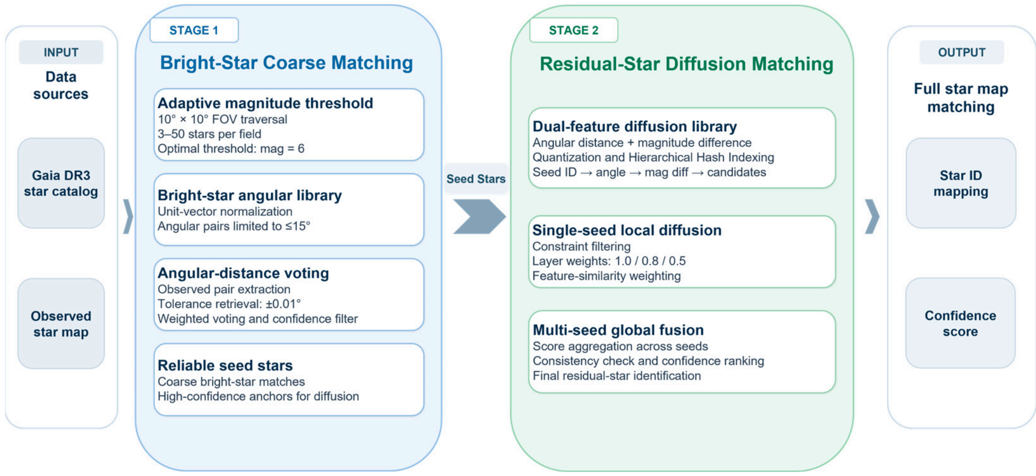

Figure 1. Overall pipeline of the two-stage star catalog matching method based on magnitude stratification and seed diffusion. The inputs consist of the observed star map and the Gaia DR3 catalog. The method first performs bright-star coarse matching, followed by residual-star diffusion matching, and finally outputs the full star map matching result.

2.1. Construction of Adaptive Bright-Star Feature Library

The bright-star feature library is the core foundation of star map matching. Its construction must balance the detector's observation capabilities (limiting magnitude and field of view) with matching robustness and efficiency. Therefore, the core goal is to select a streamlined, uniformly distributed bright-star subset by adaptively determining the magnitude stratification threshold. Based on the Gaia DR3 star catalog and considering the declination constraint ($-35°$~$35°$) for high-orbit observation scenarios, this paper designs an adaptive magnitude threshold selection algorithm to accurately construct the bright-star feature library. This library then serves as the basis for subsequent bright-star coarse matching.

2.1.1. Core Principle of Adaptive Selection of Magnitude Threshold

The magnitude threshold should be selected to ensure compatibility with both the distribution characteristics of the star catalog and the detector field of view (FOV), which is $10° \times 10°$ in this study. Three criteria are considered.

First, the lower limit of the threshold should ensure that each FOV contains at least three stars. This avoids matching failure caused by an insufficient number of stars. Second, the upper limit of the threshold should ensure that each FOV contains no more than 50 stars, thereby reducing computational complexity and mitigating matching interference in overly dense star fields. Third, the traversal analysis must cover the full catalog range required for the matching task. Since this study focuses on targets in the high-orbit belt, the analyzed region is defined as right ascension from $0°$ to $360°$ and declination from $-35°$ to $35°$. This ensures that the selected threshold is applicable throughout the catalog range relevant to the target scenario.

Accordingly, an adaptive magnitude-threshold traversal algorithm is designed, and the main steps are given below.

1. Data preprocessing: Load star catalog data, extract core parameters (star ID, right ascension (RA), declination (Dec), and magnitude (mag)), and filter out records with null values.
2. Field-of-view parameter configuration: Adopt a $10^\circ \times 10^\circ$ field of view with a 1° sliding step to scan the entire target equatorial belt, covering right ascension from 0° to 360° and declination from -35° to $+35^\circ$. Treat the right ascension direction as periodic to ensure continuous coverage across the $0^\circ/360^\circ$ boundary.
3. Magnitude threshold traversal: Set a test range of 5–7 magnitudes with a 0.1-magnitude step. For each threshold, filter the bright-star subset (mag $\leq$ threshold), traverse all sliding fields, and count the minimum, maximum, and average star numbers per field, as well as the proportion of fields meeting the target range.
4. Optimal threshold determination: Select the threshold ensuring 3–50 stars in all fields, balancing matching stability with computational efficiency.

Ultimately, a magnitude threshold of 6 is identified as optimal, which stably maintains the number of bright stars per field in the range of 3–50 with an average of 14 stars; this threshold is determined by analyzing the variation in the number of stars within the field of view under different thresholds as shown in Figure 2a, with the corresponding star count distribution illustrated by the histogram in Figure 2b, and the stars selected under this optimal magnitude threshold exhibit a well-distributed spatial pattern across the field of view as presented in Figure 3. It should be emphasized that the magnitude threshold of 6 is used only for the construction of the offline Gaia bright-star feature library. The observed bright-star subset used in the online coarse-matching stage is selected by brightness ranking to form a candidate pool.

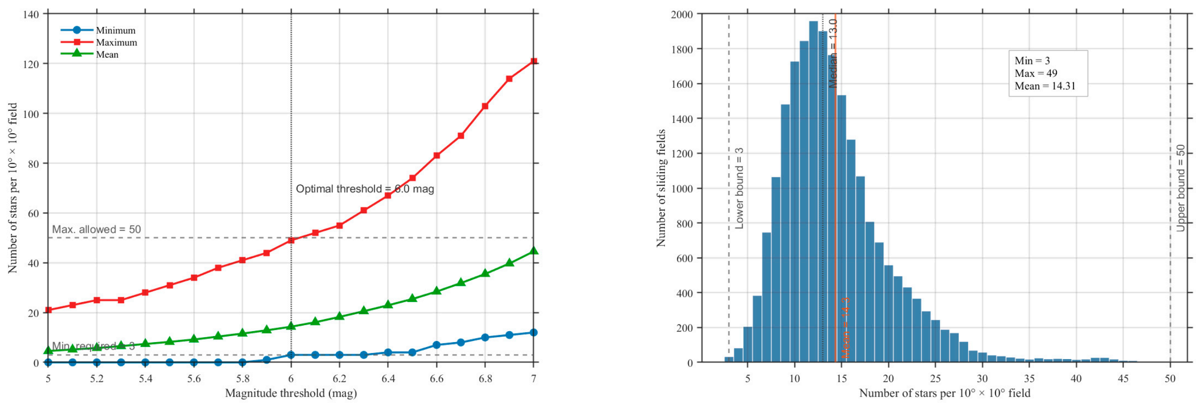

(**a**) (**b**)

Figure 2. Selection process of the magnitude threshold. (**a**) Maximum, minimum, and average number of stars within the field of view under different magnitude thresholds, indicating that a magnitude of 6 is the optimal threshold; (**b**) histogram of the star count distribution under the optimal magnitude threshold.

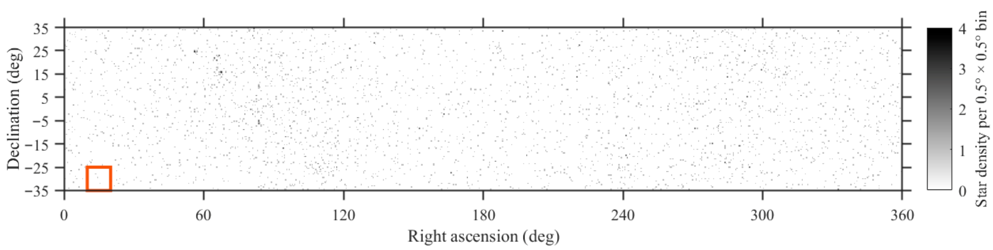

Figure 3. Spatial distribution of stars selected under the optimal magnitude threshold.

2.1.2. Construction of Bright-Star Angular-Distance Library

After bright-star selection, pairwise angular distances are computed for all valid catalog bright-star pairs and quantized to form an indexed angular-distance library. The angular distance between two catalog bright stars is calculated from their normalized celestial direction vectors, and only pairs within the predefined angular range are retained. Quantized angular-distance labels are then used to organize the feature entries into an index table, enabling rapid retrieval of candidate bright-star correspondences during the coarse-matching stage. This library supports the voting-based bright-star matching procedure described below. The formula for calculating the angular distance is given as follows:

$$\begin{cases} \cos\theta_{ij} = \vec{v}_i \cdot \vec{v}_j = \sum\limits_{d=1}^{3} v_{i,d} \cdot v_{j,d} \\ \theta_{ij} = \arccos\left(\cos\theta_{ij}\right) \times \dfrac{180^{\circ}}{\pi} \end{cases} \tag{1}$$

where θ_{ij} is the angular distance between star$_i$ and star$_j$, $\vec{v}_i$ and $\vec{v}_j$ are the unit vectors of the two stars, and $v_{i,d}$ represents the d-th dimension component of $\vec{v}_i$. An upper limit of 15° for angular distance is set based on the field of view of the telescope to filter out invalid star pairs.

All star pairs are sorted by the quantized value of the angular distance between stars, and an index table structured as quantized value–start position–end position is established. Each entry in the table records the start and end positions of star pairs with identical quantized values within the feature library.

2.2. Bright-Star Matching Algorithm Based on Angular-Distance Voting

Bright stars act as core anchor points for star map matching, and their matching accuracy directly dictates the performance of subsequent residual-star diffusion matching. Leveraging the geometric invariance of angular distances, a voting-based algorithm is adopted to achieve matching. The detailed implementation steps are as follows:

For the observed star map, a brightness-ranked candidate pool is first generated. The brightest 2% of the detected stars are selected as observed bright-star candidates, denoted as $O = \{o_1, o_2, \ldots, o_n\}$, where n is the number of selected candidates. This 2% rule is not intended to be equivalent to the magnitude threshold of 6. Rather, it is used to ensure that the possible observed counterparts of the catalog bright stars are included in the online coarse-matching stage. It should be noted that saturated stars are excluded from this candidate pool because their measured brightness values may no longer reliably reflect their true relative intensities. Using celestial sphere direction vectors converted from pixel coordinates, angular distances of all observed bright-star pairs are computed to construct the observed angular-distance matrix θ_{obs}:

$$\theta_{\text{obs}}(i,j) = \arccos\left(\vec{v}_{o_i} \cdot \vec{v}_{o_j}\right) \times \frac{180^{\circ}}{\pi}(i < j) \tag{2}$$

where $\vec{v}_{o_i}$ is the unit direction vector of the i-th observed bright star. The matrix is sorted by angular distance in ascending order.

Based on the quantized angular-distance index of the bright-star feature library, an angular-distance tolerance δ = 0.01° is set for each observed star pair angular distance θ_{obs}. All catalog star pairs satisfying $|\theta_{\text{cat}} - \theta_{\text{cos}}| \leq \delta$ are retrieved, enabling rapid localization of potential catalog star pair matches.

$$\mathbb{P} = \{(p,q) | \theta_{\text{cat}}(p,q) \in [\theta_{\text{obs}} - \delta, \theta_{\text{obs}} + \delta]\} \tag{3}$$

A voting score matrix S of size $n \times m$ is initialized (where m is the total number of bright stars in the catalog), with all elements set to 0. For each matched pair of observed star pairs (o_i, o_j) and catalog star pairs (p, q), a weighted voting rule is applied.

It should be noted that star pairs are treated as unordered pairs in the voting process because angular distance is symmetric. Therefore, for each observed bright-star pair and each catalog bright-star pair satisfying the angular-distance tolerance, both possible pair-to-pair permutations are considered during voting. This prevents valid correspondences from being missed. The incorrect permutation, if any, is subsequently suppressed by the accumulated voting scores.

A vote count of 1 is added to both $S_{i,p}$ and $S_{j,q}$ if their angular distances match; scores are accumulated for multiple matched groups. No votes are assigned to star pairs exceeding the angular-distance tolerance. In this study, a Gaussian-like weight is adopted as follows:

$$\omega_b(d) = \omega_{\min} + (1 - \omega_{\min}) \exp\left(-\frac{d^2}{2\sigma_b^2}\right) \tag{4}$$

where d denotes the angular distance of the bright-star pair, $\omega_{\min}$ is the lower bound of the voting weight, and σ_b is the decay scale of the Gaussian-like function. This design is motivated by the fact that, in a large-field optical system, long-baseline angular relations are more susceptible to residual field distortion, centroiding uncertainty, and edge-of-field optical errors, whereas short-distance relations generally provide more stable local geometric constraints.

The maximum value $S_{\max,i} = \max(S_{i,:})$ is extracted for each row of the score matrix S and the matching confidence is calculated as

$$C_i = \frac{S_{\max,i}}{\sum\limits_{j=1}^{m} S_{i,j}} \tag{5}$$

Finally, all valid matches with C(i) $\geq$ 0.6 are output in the format of observed bright-star ID, catalog bright-star ID and confidence.

2.3. Construction of Diffusion Feature Library for Remaining Stars

To support fine-grained matching of residual stars after bright-star matching, we construct a diffusion feature library that jointly encodes geometric and photometric relations between catalog bright stars and surrounding residual stars. Unlike the bright-star library, which is primarily designed for global coarse matching, the diffusion feature library is designed for local candidate retrieval centered on seed stars. The key idea is to precompute, offline, for each catalog bright star, the dual-feature relations between that bright star and all remaining catalog stars located within the observable field-of-view region. During online matching, once a bright star has been successfully matched and becomes a seed star, its corresponding preconstructed sub-library is directly invoked. In this way, the library construction is decoupled from online diffusion, and no additional adaptive estimation of the residual-star diffusion boundary is required at runtime. This design preserves global completeness while substantially reducing online search complexity.

2.3.1. Offline Local Sub-Library Generation Centered on Catalog Bright Stars

For each catalog bright star selected in Section 2.1, a local residual-star sub-library is constructed offline. The bright star serves as the reference center, and all other catalog stars falling within the predefined field-of-view support region are treated as candidate residual stars. For every bright-star–residual-star pair, two complementary descriptors are computed: the angular distance, which characterizes their relative geometric configuration on the celestial sphere, and the magnitude difference, which characterizes their relative photometric relation. The local sub-library associated with each catalog bright star therefore contains not only the identities of surrounding residual stars, but also the pairwise dual-feature descriptors required for subsequent online retrieval. Because all bright stars are processed offline in advance, the online diffusion stage only needs to access the sub-library corresponding to a matched seed star, rather than reconstructing a candidate region dynamically. This redefinition also clarifies the distinction between catalog bright-star IDs, which organize the offline library, and seed-star IDs, which arise only after online bright-star matching and are used to query the precomputed catalog sub-libraries.

2.3.2. Photometric Basis of Magnitude Difference

In addition to angular distance, we introduce magnitude difference as a complementary photometric constraint. According to Pogson's relation, stellar magnitude is logarithmically related to observed brightness.

$$mag = -2.5\lg E + C \tag{6}$$

where mag is the observed magnitude, E is the star's illuminance (brightness), and C is the observation system constant. From this, the magnitude difference between two stars is derived as

$$\Delta m_{ij} = mag_i - mag_j = -2.5\lg\frac{E_i}{E_j} \tag{7}$$

Consequently, the magnitude difference between two stars depends on their relative brightness rather than on the absolute photometric zero point of the observation system. This property makes magnitude difference well suited for residual-star matching, because it is more robust to global photometric shifts caused by exposure settings, atmospheric attenuation, or instrument bias. By coupling magnitude difference with angular distance, the proposed diffusion feature library integrates geometric distinctiveness and photometric stability within a unified retrieval framework.

It should be noted that the image magnitude used in this study is not treated as a strictly calibrated Gaia G-band magnitude before matching. In practical observations, the measured brightness of a star is affected by the detector response, exposure time, atmospheric transparency, sky background, and the spectral response of the optical system. Therefore, the Gaia G magnitude is used as the catalog-side reference magnitude, while the image-side brightness is mainly used in a relative sense. In the residual-star diffusion stage, the algorithm uses the magnitude difference between a seed star and a residual star, rather than the absolute magnitude of a single star. This relative formulation reduces the influence of frame-level exposure changes and global photometric zero-point shifts, because stars in the same image are affected by nearly the same exposure setting and overall transparency condition.

The passband of the observation system is not exactly identical to the Gaia G band. As a result, stars with different colors may show small systematic differences between their Gaia magnitudes and their measured image brightness. In this work, no explicit color-band transformation is applied; instead, the magnitude-difference feature is used as a soft auxiliary constraint together with the angular-distance constraint and the multi-seed consistency check. Possible errors caused by color-band mismatch, atmospheric extinction, background fluctuation, and local photometric uncertainty are therefore absorbed by the magnitude-difference tolerance and the weighting function. This design prevents the photometric term from dominating the final matching decision while still allowing it to reduce candidate ambiguity in dense star fields.

2.3.3. Quantization of Dual Features and Hierarchical Hash Indexing

Direct retrieval in a continuous dual-feature space is inefficient and prone to excessive redundancy. We therefore discretize both angular distance and magnitude difference using a fixed quantization step and organize the resulting feature pairs into a hierarchical hash index. Let $q_d(s,r)$ and $q_{\Delta m}(s,r)$ denote the quantized angular-distance label and quantized magnitude-difference label, respectively, for a catalog bright star s and a candidate residual star r. The diffusion feature library is then represented as a mapping

$$(s, q_d,\ q_{\Delta m}) \to \{r_1, r_2, \ldots, r_k\}, \tag{8}$$

In this formulation, the value is not represented by a single star identity, but by a set of candidate residual-star IDs satisfying the same quantized dual-feature constraints. This representation captures the inherent ambiguity of discretized retrieval and is consistent with the subsequent voting-based disambiguation strategy.

The hierarchical index comprises three levels. The first level is organized by catalog bright-star ID, which partitions the full residual-star library into independent local sub-libraries. The second level partitions each sub-library according to quantized angular-distance labels, thereby imposing a geometric constraint and rapidly reducing the search range. The third level further partitions the candidates within each angular-distance bucket according to quantized magnitude-difference labels, thereby introducing a complementary photometric constraint. The leaf nodes of the hierarchy store candidate residual-star ID sets. An illustrative example is

$$S001 \to \{234 \to \{123 \to [D001, D003]\}, 356 \to \{215 \to [D002]\}\}, \tag{9}$$

where $S001$ denotes the catalog bright star, the intermediate numeric labels denote quantized angular distance and quantized magnitude difference, and the terminal lists denote candidate residual-star IDs.

Importantly, this indexing strategy should be understood as a neighborhood-bucket retrieval mechanism rather than an exact single-key lookup. During online matching, observed dual features are first quantized and then expanded to a local tolerance neighborhood in the discretized feature space. Candidate residual stars are retrieved from all buckets whose labels fall within the allowed angular-distance and magnitude-difference ranges. The retrieved candidate set is then scored and filtered during the subsequent seed-diffusion voting stage. This design preserves the computational advantages of hash-based indexing while remaining compatible with the tolerance-based nature of practical star map matching.

2.4. Seed Diffusion Voting Matching for Remaining Stars

Following bright-star coarse matching, the validated bright-star correspondences are treated as seed stars and used to activate the corresponding diffusion sub-libraries constructed offline. Residual-star matching is then performed in two stages: single-seed local diffusion and multi-seed global fusion. In the first stage, each seed star independently retrieves candidate residual stars from its local sub-library under dual-feature neighborhood constraints and assigns weighted local scores according to diffusion distance and feature consistency. In the second stage, the local scores contributed by multiple seed stars are fused globally, and cross-seed consistency is used to suppress local ambiguity and correct isolated mismatches. This two-stage design is consistent with the structure of the diffusion feature library: the library provides candidate residual-star sets at the retrieval level, whereas the voting mechanism resolves ambiguity at the decision level.

2.4.1. Single-Seed-Point Initial Diffusion: Local Accurate Retrieval

Single-seed initial diffusion constitutes the fundamental unit of the residual-star matching procedure. For a given matched bright star s serving as a seed, the observed angular distance and magnitude difference between the seed and an observed residual star o_i are first computed. Candidate stars are then retrieved from the corresponding offline diffusion sub-library by enforcing dual-feature neighborhood constraints:

$$\left| d^{obs}(o_i, s) - d^{cat}(r, s) \right| \leq \varepsilon_d, \tag{10}$$

$$\left| \Delta m^{obs}(o_i, s) - \Delta m^{cat}(r, s) \right| \leq \varepsilon_m, \tag{11}$$

where r denotes a candidate residual star in the catalog sub-library associated with seed s, $d^{obs}(o_i, s)$ and $\Delta m^{obs}(o_i, s)$ are the observed angular distance and magnitude difference, and $d^{cat}(r, s)$ and $\Delta m^{cat}(r, s)$ are the corresponding catalog-derived quantities. The angular-distance tolerance ε_d and magnitude-difference tolerance ε_m are selected according to the expected measurement-error scale of the adopted wide-field observation system. The angular-distance tolerance is mainly related to the angular resolution of the telescope, centroid extraction uncertainty, residual optical distortion, edge-field imaging errors, and feature quantization errors. It is used as a candidate-retrieval tolerance rather than as the final matching-accuracy requirement. Therefore, it should be sufficiently large to prevent correct candidates from being removed at the retrieval stage, but not so large that excessive ambiguous candidates are introduced in dense star fields. The magnitude-difference tolerance is selected according to the expected relative photometric uncertainty of unsaturated star images. The adopted tolerance is chosen to allow normal relative-brightness fluctuations while still suppressing candidates with obviously inconsistent photometric relationships.

To improve discrimination among candidates returned by the neighborhood buckets, a hierarchical gradient weighting strategy is introduced. The initial score assigned by seed star s to candidate star r for observed residual star o_i is defined as

$$V_s(o_i, r) = w_{\text{layer}}(o_i, s) \cdot w_{\text{feature}}(o_i, r \mid s) \tag{12}$$

where w_{layer} denotes the diffusion-layer weight and w_{feature} denotes the feature-matching weight.

The diffusion-layer weight is used to describe the decreasing reliability of a residual star as its angular distance from the seed star increases. We adopt the same Gaussian-like decay function as that used in the bright-star voting stage:

$$w_{\text{layer}} = \omega_{\text{min}} + (1 - \omega_{\text{min}}) \exp\left(-\frac{d^2}{2\sigma_l^2} \right), \tag{13}$$

where d denotes the angular distance between the seed star and the observed residual star, ω_{min} is the lower bound of the diffusion weight, and σ_l is the decay scale of the diffusion process. This design reflects the local-diffusion assumption of the proposed method: residual stars closer to a reliable seed star are generally constrained by more stable local geometric relations, whereas stars farther from the seed are more likely to be affected by accumulated distortion, local ambiguity, and false-star interference. Therefore, the diffusion weight is designed as a monotonically decreasing function of the seed-to-residual angular distance.

As illustrated in Figure 4, the angular-distance-dependent diffusion mechanism allocates different weights to residual stars according to their angular distances from the seed stars. Analogous to a pigment diffusion process, stars that are closer to the seed stars are assigned higher weights.

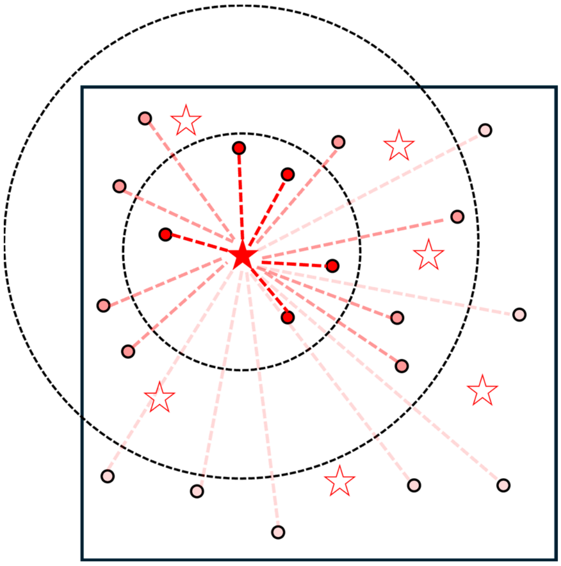

Figure 4. Schematic illustration of the diffusion-layer weight. Different diffusion layers are assigned varying weights according to the angular distance. The process is analogous to pigment diffusion, where the pentagram markers denote seed stars and the circular markers represent residual stars. The color intensity indicates the magnitude of the weights, with darker colors corresponding to higher weights.

The feature-matching weight quantifies the agreement between observed and catalog dual features. Let

$$\delta_d = d^{obs}(o_i, s) - d^{cat}(r, s), \delta_m = \Delta m^{obs}(o_i, s) - \Delta m^{cat}(r, s), \tag{14}$$

where δ_d and δ_m denote the angular-distance deviation and magnitude-difference deviation, respectively. A larger deviation implies weaker consistency between the observed residual star and the candidate catalog star. Accordingly, the feature-matching weight is defined as a joint attenuation function of the two deviations:

$$w_{\text{feature}} = \exp\left(-\frac{\delta_d^2}{2\sigma_d^2}\right) \cdot \exp\left(-\frac{\delta_m^2}{2\sigma_m^2}\right) \tag{15}$$

where σ_d and σ_m denote the standard deviations of angular-distance and magnitude-difference deviations, respectively. The standard deviations used in the weighting function are obtained from the expected measurement-error level of the adopted observation system. For different instruments or exposure settings, these parameters can be adjusted according to the corresponding imaging accuracy and photometric stability.

For all candidate stars satisfying the dual-feature retrieval constraints, the weighted score $V_s(o_i, r)$ serves as the single-seed initial voting result. Candidates that fail either the geometric or photometric constraint are assigned a score of zero and discarded directly. Therefore, single-seed initial diffusion performs local candidate generation and local confidence assignment simultaneously, laying the foundation for the subsequent multi-seed fusion stage.

2.4.2. Multi-Seed Diffusion Fusion: Global Cross-Validation

Although single-seed diffusion provides efficient local retrieval, it remains vulnerable to local ambiguity, bright-star matching error, and feature noise. To improve robustness, the initial scores generated by all seed stars are fused into a global voting matrix, followed by multi-anchor consistency verification and confidence-based decision making.

Let S denote the set of seed stars participating in diffusion. For each observed residual star o_i and catalog candidate star r, the global voting score is defined as the sum of all single-seed contributions:

$$G(o_i, r) = \sum_{s \in S} V_s(o_i, r) \tag{16}$$

This matrix aggregates local evidence from multiple anchors and converts local retrieval outcomes into global matching features. To suppress candidates supported by only one unreliable seed and promote candidates consistently validated by multiple seeds, a multi-anchor consistency coefficient is introduced. For each candidate star r, let n_r be the number of seed stars that provide non-zero support for the pair (o_i, r). The consistency coefficient is defined as

$$C_{\text{cons}}(o_i, r) = \frac{n_r}{|S|} \tag{17}$$

where $|S|$ is the total number of seed stars involved in diffusion. A minimum consistency threshold τ_c is then imposed. Candidates satisfying

$$C_{\text{cons}}(o_i, r) \geq \tau_c \tag{18}$$

receive an additional consistency enhancement, whereas candidates failing this condition are down-weighted or eliminated. The updated global score can therefore be written as

$$G'(\mathrm{o_i}, \mathrm{r}) = \mathrm{G}(\mathrm{o_i}, \mathrm{r}) \cdot \varphi(\mathrm{C_{cons}}(\mathrm{o_i}, \mathrm{r})) \tag{19}$$

where $\varphi(\cdot)$ is a monotonic consistency enhancement function. This mechanism implements global cross-validation among multiple seed stars and suppresses mismatches that are locally plausible but globally unsupported.

2.4.3. Confidence Ranking and Final Decision

After global fusion and consistency enhancement, the final match for each observed residual star is determined by confidence ranking. In the implementation, the final decision is not performed as an independent row-wise selection for each observed residual star. Instead, a one-to-one assignment constraint is imposed after confidence ranking. If multiple observed residual stars select the same catalog candidate, the assignment with the highest global score and confidence is retained, whereas the conflicting lower-confidence assignments are reassigned to their next feasible candidates. In this way, each observed residual star is matched to at most one catalog star, and each catalog star is assigned to at most one observed star.

$$r_i^* = \arg\max_r G'(\mathrm{o_i}, \mathrm{r}) \tag{20}$$

The corresponding matching confidence is defined as

$$\mathrm{Conf}(o_i) = \begin{cases} \frac{\max_r G'(o_i, r)}{\sum_r G'(o_i, r)} & \sum_r G'(o_i, r) > 0 \\ 0 & \sum_r G'(o_i, r) = 0 \end{cases} \tag{21}$$

This confidence value measures the relative dominance of the best candidate over all competing candidates. Higher confidence indicates stronger uniqueness and lower mismatch risk. If $\mathrm{Conf}(o_i)$ exceeds a preset threshold τ_f, the match $o_i \rightarrow r_i^*$ is accepted; otherwise, the residual star is treated as unmatched or reserved for secondary compensation.

Overall, the proposed seed-guided diffusion voting mechanism transforms the residual-star matching task into a hierarchical process consisting of local candidate retrieval, local weighted voting, global multi-anchor fusion, and a confidence-based final decision. By coupling an offline dual-feature diffusion library with online seed-driven neighborhood-bucket retrieval and global voting fusion, the method achieves efficient and robust full star map matching in large-field dense star scenarios.

3. Results and Discussion

To comprehensively evaluate the proposed star map matching algorithm, the experimental dataset is divided into two parts: a simulation dataset and a real observation dataset. Following the control-variable principle, the dataset design separately examines the effects of positional noise, false-star interference, and star density on algorithm performance. Specifically, simulated star maps are used to assess the algorithm under controlled conditions, while real observation data are employed to validate its practical applicability.

3.1. Dataset Design

The simulation dataset is constructed based on the Gaia DR3 star catalog and contains a total of 18,000 star maps. According to the experimental objectives, it is further divided into three independent test subsets. The ground-truth correspondences are obtained directly during the star map generation process. Each simulated star is generated from a known Gaia DR3 catalog entry, and its catalog source ID is retained as the ground-truth label. All subsets share the same basic parameters: an image resolution of 4096×4096 pixels, a pixel size of 9 μm, a reference focal length of 200 mm, a stellar declination range from -35° to 35° covering the equatorial belt, and a star point gray distribution that follows a Gaussian model. The detailed design is as follows.

The star-density impact test subset contains 6000 star maps. In this subset, gradient variations in star density are generated by adjusting the limiting magnitude during simulation, thereby covering scenarios with different stellar densities. Six magnitude levels are defined, ranging from magnitude 7, with an average of 44.6 stars per field of view, to magnitude 12, with an average of 6043.2 stars per field of view. For each magnitude level, 1000 random star maps are generated.

The position noise resistance test subset contains 6000 star maps. In this subset, the simulation is conducted under the limiting-magnitude condition of 9 mag, and Gaussian noise with a mean of 0 pixels and a variance ranging from 0 to 1.5 pixels is added to the star point coordinates. This design is intended to evaluate how recognition accuracy changes under different levels of positional disturbance.

The false-star resistance test subset also contains 6000 star maps. In this subset, the simulation is conducted under the limiting-magnitude condition of 9 mag, and no positional noise is added. On this basis, 0 to 50 false stars are randomly introduced to verify the robustness of different star recognition algorithms against false-star interference. Each false-star level contains 1000 star maps. The false stars are randomly distributed across the field of view, and their gray levels follow the statistical characteristics of real star points.

The measured dataset is obtained from a $10^\circ \times 10^\circ$ large-field telescope and contains 1000 real observational frames covering the equatorial belt. The hardware parameters are consistent with those of the simulation dataset, including an image resolution of 4096×4096 pixels, a pixel size of 9 μm, and a focal length of 200 mm. The exposure time of each frame is 2 s, and the limiting magnitude reaches approximately 12.5 mag. On average, about 1000 stars are extracted from each measured frame. This dataset is used to verify the practical engineering applicability of the proposed algorithm in complex optical observation scenarios. For the measured dataset, the correctness of the matching results is verified by astrometric consistency. After the algorithm outputs the star correspondences, a plate model is fitted between the image coordinates of the matched stars and the celestial coordinates of the corresponding Gaia DR3 catalog stars. Matches with residuals within the preset tolerance after iterative outlier rejection are regarded as correct. This provides an objective verification criterion for real observational data.

3.2. Experimental Results and Analysis

Two core evaluation metrics are adopted in the experiments to comprehensively assess the performance of the proposed algorithm. The first is the matching success rate (MSR), which is defined as the ratio of the number of correctly matched observed stars to the total number of extracted observed stars. The second is the average matching time (AMT), which represents the average time required to complete the processing of a single star map, from feature extraction to final matching, measured in seconds.

To demonstrate the effectiveness of the proposed method, three representative algorithms are selected as benchmark methods for comparison: the Pyramid algorithm [26], the Geometric Voting (GMV) algorithm [27], and the Rotation-Invariant Additive Vector (RIAV) algorithm [28]. The comparison methods were selected according to representativeness and reproducibility under identical experimental conditions. Pyramid, GMV, and RIAV represent classical subgraph-based, geometric-voting, and rotation-invariant matching strategies, and their main algorithmic procedures can be consistently implemented on the same simulated and measured datasets used in this study.

All experiments are conducted on a platform equipped with an Intel Xeon Gold 5218 CPU (2.3 GHz, 64 GB RAM) and an NVIDIA Quadro RTX 5000 GPU (48 GB memory), with MATLAB 2025b used as the software environment.

3.2.1. Impact of Star Point Density on Algorithm Performance

Star point density is the core factor affecting the performance of dense star field matching algorithms. Table 1 shows the MSR and AMT of each algorithm under different star point density levels, and the key findings derived from the experimental results are as follows:

Table 1. Performance of each algorithm under different star point densities.

Average Number of Stars in Field of View	Algorithm	Matching Success Rate (%)	Average Matching Time (s)
44.6	Pyramid	98.2	0.186
	GMV	98.1	0.224
	RIAV	98.5	0.083
	Proposed	98.2	0.079
129.8	Pyramid	95.2	0.352
	GMV	94.5	0.586
	RIAV	92.2	0.157
	Proposed	98.5	0.142
363.2	Pyramid	91.6	0.785
	GMV	90.8	1.453
	RIAV	88.5	0.324
	Proposed	98.3	0.287
971.5	Pyramid	87.4	1.893
	GMV	80.5	3.875
	RIAV	68.7	0.896
	Proposed	97.9	0.764

Table 1. *Cont.*

Average Number of Stars in Field of View	Algorithm	Matching Success Rate (%)	Average Matching Time (s)
2474.1	Pyramid	84.9	4.267
	GMV	75.2	9.684
	RIAV	49.2	2.458
	Proposed	97.1	1.983
6043.2	Pyramid	80.2	11.584
	GMV	71.5	26.457
	RIAV	32.5	7.892
	Proposed	94.7	6.238

In sparse star field scenarios (44.6 stars), all algorithms maintain high matching success rates (≥98.1%), and the proposed method achieves the shortest AMT (0.079 s), which is 0.004 s lower than RIAV (0.083 s) with the second highest efficiency, showing a slight advantage in real-time performance under low computational complexity.

With the gradual increase in star point density, the performance of traditional algorithms degrades drastically and shows poor scalability: the MSR of Pyramid, GMV and RIAV drops to 80.2%, 71.5% and 32.5% respectively at the ultra-dense star field level (6043.2 stars); the AMT of GMV surges exponentially to 26.457 s (about 118 times that of the sparse star field), and Pyramid's AMT also reaches 11.584 s, which is caused by the massive redundant matching and computational complexity increase in traditional algorithms in dense star fields.

The proposed method maintains excellent accuracy and efficiency scalability in the whole density range: the MSR remains above 94.7% even at the ultra-dense star field level, and the AMT only increases to 6.238 s (about 79 times that of the sparse star field), which is far lower than Pyramid and GMV (about 1/4 of GMV). The performance of the algorithms under different star point densities is listed in Table 1, while the corresponding comparative results are illustrated in Figure 5.

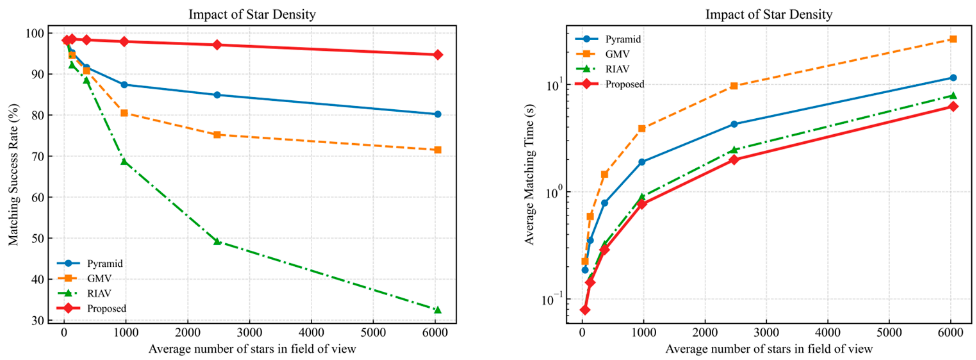

(**a**) (**b**)

Figure 5. Performance comparison of the algorithms under different star point densities: (**a**) matching success rate (MSR); (**b**) average matching time (AMT).

The strong density robustness suggests that the improvement is structurally linked to the feature design rather than to parameter tuning alone. Traditional methods such as triangle matching, grid matching, and additive vector schemes were developed primarily for star-sensor regimes in which the number of stars per frame is limited and the catalog search space remains relatively sparse. Under those conditions, invariant geometric patterns are highly effective. However, when the limiting magnitude reaches the range typical of astronomical telescopes and surveillance optics, the number of candidate correspondences grows rapidly and many local patterns become non-unique. The present study addresses this shift by introducing a dual-feature residual library based on angular distance and magnitude difference, indexed through a three-level hash structure. This combination is important because angular distance preserves geometric invariance, whereas magnitude difference supplies an additional photometric discriminator that remains relatively stable under global illumination shifts. The resulting gain in uniqueness likely explains why the proposed method exhibited a much flatter efficiency-loss curve than Pyramid, GMV, and RIAV as star density increased. In that sense, the method extends earlier angular-feature-based approaches by showing that geometry alone is often insufficient once the scene enters the high-density, high-redundancy regime.

3.2.2. Anti-Position Noise Performance of Algorithms

Position noise is a common interference in optical star map observation, which is mainly caused by telescope optical distortion and image sensor noise. Table 2 shows the performance of each algorithm when the position Gaussian noise increases from 0 to 1.5 pixels (based on 9 mag limiting magnitude and 363.2 stars in the field of view), and the key findings are as follows:

Table 2. Performance of each algorithm under different position noise levels.

Position Noise (Pixel)	Algorithm	Matching Success Rate (%)	Average Matching Time (s)
0	Pyramid	91.6	0.785
	GMV	90.8	1.453
	RIAV	88.5	0.324
	Proposed	98.3	0.287
0.3	Pyramid	91.5	0.792
	GMV	90.4	1.567
	RIAV	88.4	0.331
	Proposed	98.2	0.293
0.6	Pyramid	91.4	0.806
	GMV	89.6	1.724
	RIAV	88.4	0.345
	Proposed	98.3	0.305
0.9	Pyramid	91.2	0.823
	GMV	89.1	1.958
	RIAV	88.3	0.368
	Proposed	97.9	0.314
1.2	Pyramid	91	0.857
	GMV	88.5	2.236
	RIAV	88.3	0.396
	Proposed	97.6	0.347
1.5	Pyramid	90.5	0.884
	GMV	88	2.568
	RIAV	88.2	0.427
	Proposed	97.3	0.372

The proposed method exhibits superior robustness to positional noise: with the noise intensity increasing from 0 to 1.5 pixels, the MSR only decreases slightly from 98.3% to 97.3% (a decrease of only 1 percentage point), and the AMT only increases slightly from 0.287 s to 0.372 s, with almost no significant fluctuation in both accuracy and efficiency.

Traditional algorithms show obvious performance defects under noise interference: Pyramid and GMV have a continuous decline in MSR (GMV drops by 2.8 percentage points), and their AMT increases gradually (GMV's AMT rises to 2.568 s) due to repeated verification and correction of wrong matching results; RIAV can maintain a relatively stable

MSR (above 88.2%), but its AMT is consistently lower than the proposed method under the same noise level. The corresponding comparative results are illustrated in Figure 6.

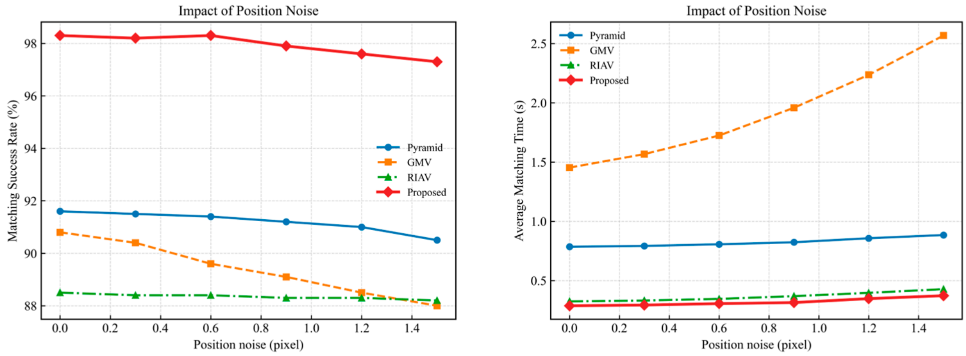

(**a**) (**b**)

Figure 6. Performance comparison of the algorithms under different position noise levels: (**a**) matching success rate (MSR); (**b**) average matching time (AMT).

The noise experiments provide additional evidence that the algorithmic stability originates from the weighting and fusion strategy rather than from strict feature tolerances. The relatively small decline in matching success rate as positional noise increased to 1.5 pixels indicates that the method does not rely excessively on any single observation of inter-star geometry. Instead, the weighted bright-star voting stage increases the contribution of short-baseline, high-reliability star pairs, while the residual-star diffusion stage aggregates evidence from multiple anchors and tolerates moderate perturbations in both angular and photometric measurements. This behavior is important because real optical surveillance systems are affected by centroiding error, optical distortion, platform jitter, atmospheric turbulence, and focal-plane nonuniformity. Methods that treat each local pattern as an isolated rigid signature are more vulnerable to these factors, because one disturbed feature may invalidate the entire match chain. By contrast, the present seed-diffusion strategy distributes evidence across multiple anchors and thereby reduces sensitivity to local measurement noise. This interpretation is consistent with recent graph-based and voting-based star identification methods, which also report improved robustness when matching evidence is propagated or accumulated rather than decided from a single descriptor [20,24].

3.2.3. Anti-False-Star Interference Performance of Algorithms

False stars are mainly caused by cosmic ray interference and image background noise, which are important factors leading to mismatching in dense star fields. Table 3 shows the performance of each algorithm when the number of random false stars increases from 0 to 50 (based on 9 mag limiting magnitude and 363.2 stars in the field of view), and the key findings are as follows:

Table 3. Performance of each algorithm under different numbers of false stars.

False Stars	Algorithm	Matching Success Rate (%)	Average Matching Time (s)
0	Pyramid	91.6	0.785
	GMV	90.8	1.453
	RIAV	88.5	0.324
	Proposed	98.3	0.287
10	Pyramid	91.5	0.812
	GMV	90.8	1.645
	RIAV	88.5	0.337
	Proposed	98.3	0.298

Table 3. *Cont.*

False Stars	Algorithm	Matching Success Rate (%)	Average Matching Time (s)
20	Pyramid	91.6	0.846
	GMV	90.8	1.768
	RIAV	86.3	0.352
	Proposed	98.4	0.314
30	Pyramid	91.5	0.889
	GMV	90.7	2.142
	RIAV	78.4	0.376
	Proposed	98.2	0.336
40	Pyramid	91.5	0.935
	GMV	90.7	2.458
	RIAV	70.3	0.403
	Proposed	98.3	0.362
50	Pyramid	91.5	0.987
	GMV	90.7	2.978
	RIAV	63.5	0.438
	Proposed	98.3	0.395

The proposed method has strong immunity to false-star interference: with the number of false stars increasing from 0 to 50, the MSR is stably maintained at about 98.3% (the fluctuation is less than 0.2 percentage points), and the AMT only increases slightly from 0.287 s to 0.395 s, and is almost unaffected by the increase in false stars.

Traditional algorithms show obvious vulnerability to false-star interference, especially RIAV: its MSR drops sharply from 88.5% to 63.5% (a decrease of 25 percentage points) with the increase in false stars, because it is difficult to filter the false-star matching results generated by dense false stars in the single-feature matching process; although Pyramid and GMV can maintain a relatively stable MSR, their AMT increases significantly (GMV's AMT rises to 2.978 s), and the real-time performance is far lower than the proposed method. The performance of the algorithms under different numbers of false stars is listed in Table 3, while the corresponding comparative results are illustrated in Figure 7.

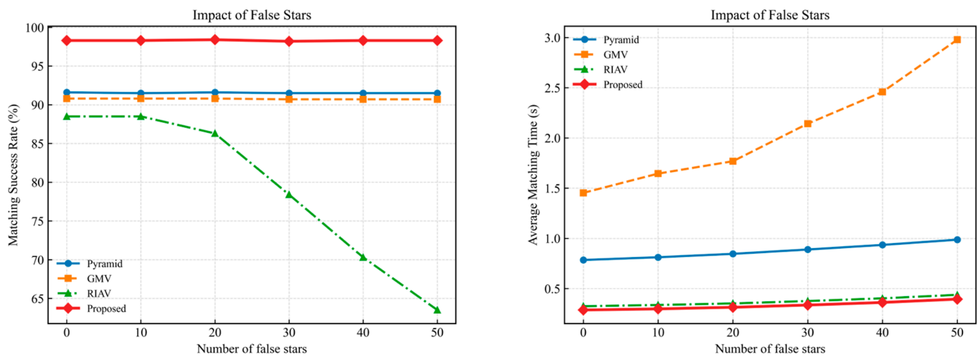

(**a**) (**b**)

Figure 7. Performance comparison of the algorithms under different numbers of false stars: (**a**) matching success rate (MSR); (**b**) average matching time (AMT).

The false-star experiments are especially relevant for SSA applications, because contamination from cosmic rays, hot pixels, background fluctuation, and unresolved artifacts is unavoidable in long-exposure or wide-field imaging. Here, the proposed framework showed almost no loss of success rate as the number of false stars increased within the tested range, which suggests that the multi-seed consistency mechanism effectively suppresses spurious local correspondences. This result highlights an important distinction from methods that depend mainly on one-shot local pattern recognition. False stars can mimic plausible local configurations, especially in dense fields, but they are much less likely to be jointly supported by multiple seed stars under both geometric and photometric constraints. The consistency-enhancement rule therefore functions as a global plausibility filter, rejecting candidates that are locally admissible but globally incompatible. This is conceptually aligned with prior work using polygon constraints [14,21], graph propagation, or cross-validation stages to improve robustness.

3.2.4. Engineering Applicability Verification Based on Measured Dataset

Engineering applicability is the key index to evaluate the practical value of the algorithm. Table 4 presents the performance of each algorithm on the measured dataset of the $10^\circ \times 10^\circ$ large-field telescope, and the key findings are as follows:

Table 4. Performance of each algorithm on measured dataset.

Algorithm	Matching Success Rate (%)	Average Matching Time (s)
Pyramid	90.6	0.942
GMV	88.7	1.681
RIAV	85.5	0.443
Proposed	96.3	0.503

The proposed method achieves the best comprehensive performance on the measured dataset: the MSR reaches 96.3%, which is 5.7, 7.6 and 10.8 percentage points higher than that of Pyramid (90.6%), GMV (88.7%) and RIAV (85.5%) respectively; the AMT is 0.503 s, which is only slightly higher than that of RIAV (0.443 s) but far lower than that of Pyramid (0.942 s) and GMV (1.681 s), realizing the balance of high accuracy and real-time performance in actual observation scenarios.

The slight decrease in the proposed method's MSR in the measured dataset compared with the simulated dataset (from 98.3% to 96.3%) is mainly caused by actual complex observation factors such as atmospheric extinction, telescope optical distortion and background light interference, which is an inevitable error in the transition from ideal simulation to actual application, and the decrease range is far lower than that of traditional algorithms, showing strong adaptability to complex actual observation environments.

The matching results for the measured star image are illustrated in Figure 8, where red circles denote matched seed stars, yellow circles indicate successfully matched residual stars, and blue dots represent residual stars that failed to be matched. The experimental results demonstrate that the method remains effective when transitioning from simulation to real images, despite inevitable reductions in performance caused by atmospheric extinction, optical distortion, and background light. The remaining gap between simulated and measured performance should therefore be interpreted as evidence of engineering realism rather than methodological fragility.

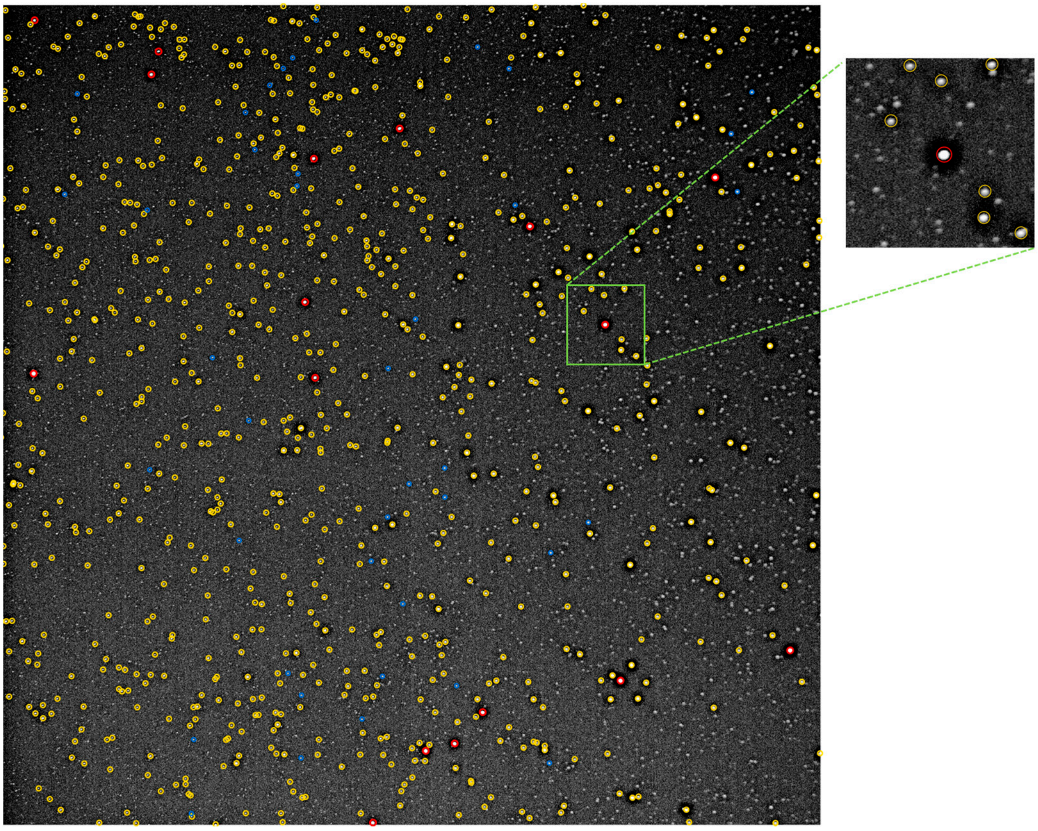

Figure 8. Matching results for the measured star image. The red circles denote the matched seed stars, the yellow circles indicate the successfully matched residual stars, and the blue dots represent the unmatched residual stars.

4. Conclusions

This study addressed a key bottleneck in large-field optical space surveillance, namely how to achieve accurate and computationally efficient star map matching when the number of detectable stars increases dramatically. The results demonstrate that the proposed two-stage framework, which combines adaptive magnitude stratification with seed-diffusion matching, consistently improved both the matching success rate and runtime performance in simulated and measured dense star scenarios. In particular, the method maintained high recognition performance under increasing star density, positional noise, and false-star interference, while remaining substantially more time-efficient than conventional geometric matching pipelines. These results suggest that the main advantage of the proposed method lies not only in its matching accuracy, but also in its superior scalability for modern large-field optical systems with high limiting magnitudes.

A central insight of this work is that dense star matching can be effectively handled through a hierarchical strategy that separates global anchoring from local propagation. The adaptive bright-star library reduces the initial combinatorial search space by selecting a sparse yet sufficiently uniform set of reliable anchor stars, thereby avoiding the rapid growth of redundant pairwise or polygonal comparisons that typically limits performance in dense fields. This mechanism explains why the proposed method was able to maintain a matching success rate above 94% even in ultra-dense scenarios with more than 6000 stars per field, whereas the benchmark methods exhibited much sharper degradation. In this framework, the bright-star stage provides robust global initialization, while the residual-star stage performs constrained local expansion around trustworthy seed stars. Compared with methods that rely solely on triangle, radial, or graph-topology descriptors, the proposed approach reduces ambiguity at the early stage and confines fine matching to a much smaller candidate space.

It should be emphasized that the contribution of this study is incremental rather than a fundamentally new matching paradigm. Recent dense-scene methods, such as the 2024 dense star map matching approach based on inter-star angular features [24], have already demonstrated the effectiveness of two-step coarse-to-fine matching and angular-feature voting in high-density scenarios. Different from such angular-feature-only strategies, the proposed method further integrates adaptive magnitude-stratified bright-star anchoring, a seed-centered residual-star diffusion library jointly constrained by angular distance and magnitude difference, and multi-seed global fusion. Therefore, the main contribution of this work lies in the task-specific integration of these components for large-field dense star scenes. Nevertheless, several limitations remain. The range of real observational conditions considered in this study is still limited, the validation depends on specific instrument configurations, and a complete end-to-end assessment of the final astrometric solution accuracy has not yet been carried out. These issues should be further investigated in future work.

Overall, the proposed framework provides a robust and efficient basis for practical dense star map matching and shows strong potential for engineering implementation in wide-field telescope systems. Future work will focus on cross-platform validation, adaptive parameter self-calibration, distortion-aware modeling, probabilistic confidence assessment, and tighter integration with downstream astrometric positioning pipelines, in order to further improve the generalizability and operational utility of the method.

Author Contributions: Conceptualization, K.Z. and Y.Z.; methodology, J.Q. and K.Z.; software, K.Z.; validation, J.Q.; formal analysis, J.Q. and C.X.; investigation, K.Z.; data curation, J.Q.; writing—original draft preparation, K.Z.; writing—review and editing, J.Q.; supervision, Y.F. and Y.Z. All authors have read and agreed to the published version of the manuscript.

Funding: This research received no external funding.

Data Availability Statement: The data used in this study are available from Baidu Netdisk. For access to the data, please contact kaiyuan_zheng@hgd.edu.cn.

Acknowledgments: We sincerely appreciate the Shanghai Astronomical Observatory for providing the essential equipment, which laid a solid foundation for the smooth progress of our research. Additionally, we would like to express our heartfelt gratitude to our laboratory coworkers. Their invaluable help and continuous support throughout the research process, including assistance with experiments and data collection, and discussion of research ideas, were crucial to the completion of this study.

Conflicts of Interest: The authors declare no conflicts of interest.

Abbreviations

The following abbreviations are used in this manuscript:

SSA	Space Situational Awareness
FOV	Field of View
Gaia DR3	Gaia Data Release 3
RA	Right Ascension
Dec	Declination
Mag	Magnitude
PCA	Principal Component Analysis
GMM	Gaussian Mixture Model
SVD	Singular Value Decomposition
MSR	Matching Success Rate

AMT	Average Matching Time
GMV	Geometric Voting
RIAV	Rotation-Invariant Additive Vector
CPU	Central Processing Unit
GPU	Graphics Processing Unit
RAM	Random Access Memory

References

1. Su, S.; Niu, W.; Li, Y.; Ren, C.; Peng, X.; Zheng, W.; Yang, Z. Dim and Small Space-Target Detection and Centroid Positioning Based on Motion Feature Learning. *Remote Sens.* **2023**, *15*, 2455. [CrossRef]
2. Zheng, K.; Xu, C.; Zhang, Y.; Qiu, J.; Wang, X. Geostationary Orbit Target Detection Based on Min-Stacking Method. *Aerospace* **2025**, *12*, 834. [CrossRef]
3. Wang, H.; Chen, S.; Shen, Z.; Zhang, T.; Zhang, G.; Zhang, X.; Lin, B.; Blake, J.A.; Yang, X. Improved space target detection and tracking via enhanced spatiotemporal representation. *Acta Astronaut.* **2026**, *245*, 471–480. [CrossRef]
4. Feuge-Miller, B.G.; Jah, M.K. A-contrario structural inference for space object detection and tracking. *Acta Astronaut.* **2022**, *200*, 86–96. [CrossRef]
5. Dave, S.; Clark, R.; Lee, R.S.K. RSOnet: An Image-Processing Framework for a Dual-Purpose Star Tracker as an Opportunistic Space Surveillance Sensor. *Sensors* **2022**, *22*, 5688. [CrossRef] [PubMed]
6. Campiti, G.; Brunetti, G.; Ciminelli, C. Detectability of potentially colliding space objects via star trackers on at-risk satellites. *IEEE Trans. Aerosp. Electron. Syst.* **2025**, *61*, 11489–11507. [CrossRef]
7. Liu, H.; Wei, X.; Li, J.; Wang, G. A star identification algorithm based on simplest general subgraph. *Acta Astronaut.* **2021**, *183*, 11–22. [CrossRef]
8. Wang, X.; Li, Z.; Xu, C.; Huo, Y.; Feng, F.; Qiu, S.; Zheng, K.; Qiu, J. Star Suppression Based on Structure of Star Groups for Geosynchronous Object Detection Using Wide-Field Telescopes. *IEEE Trans. Aerosp. Electron. Syst.* **2024**, *60*, 3160–3176. [CrossRef]
9. Zhu, Z.; Ma, Y.; Dan, B.; Liu, E.; Zhu, Z.; Yi, J.; Tang, Y.; Zhao, R. An Autonomous Global Star Identification Algorithm Based on the Fast MST Index and Robust Multi-Order CCA Pattern. *Remote Sens.* **2023**, *15*, 2251. [CrossRef]
10. Wu, S.; Sun, T.; Xing, F.; Liu, H.; Song, J.; Yu, S. Research on Full-Sky Star Identification Based on Spatial Projection and Reconfigurable Navigation Catalog. *Remote Sens.* **2025**, *17*, 1553. [CrossRef]
11. McKee, P.; Kowalski, J.; Christian, J.A. Navigation and star identification for an interstellar mission. *Acta Astronaut.* **2022**, *192*, 390–401. [CrossRef]
12. Groth, E.J. A pattern-matching algorithm for two-dimensional coordinate lists [for stellar positions]. *Astron. J.* **1986**, *91*, 1244–1248. [CrossRef]
13. Padgett, C.; Kreutz-Delgado, K. A Grid Algorithm for Autonomous Star Identification. *IEEE Trans. Aerosp. Electron. Syst.* **1997**, *33*, 202–213. [CrossRef]
14. He, X.; Zhang, L.; He, J.; Mu, Z.; Lv, Z.; Wang, J. A Voting-Based Star Identification Algorithm Using a Partitioned Star Catalog. *Appl. Sci.* **2025**, *15*, 397. [CrossRef]
15. Yuan, X.; Zhu, J.; Zhu, K.; Li, X. A Star-Identification Algorithm Based on Global Multi-Triangle Voting. *Appl. Sci.* **2022**, *12*, 9993. [CrossRef]
16. Liu, D.L.; Yang, W.B.; Liu, M.; Kang, Z.; Li, Z. Rapid star pattern matching for precisely tracking telescopes. *Opt. Precis. Eng.* **2022**, *30*, 2952–2961. [CrossRef]
17. Ramos-Alcaraz, G.E.; Alonso-Arévalo, M.A.; Núñez-Alfonso, J.M. Star-Identification System Based on Polygon Recognition. *Aerospace* **2023**, *10*, 748. [CrossRef]
18. Jiang, D.; Zhang, K.; Debeir, O. Star image recognition based on mutual star distribution. *Syst. Eng. Electron.* **2018**, *40*, 127–131.
19. Mehta, D.S.; Chen, S.S.; Low, K.S. A Rotation-Invariant Additive Vector Sequence Based Star Pattern Recognition. *IEEE Trans. Aerosp. Electron. Syst.* **2019**, *55*, 689–705. [CrossRef]
20. Kim, K. A new star identification using patterns in the form of Gaussian mixture models. *Adv. Space Res.* **2024**, *74*, 319–331. [CrossRef]
21. Wei, Y.H.; Wei, X.G.; Liu, H.; Li, J. A Star Identification Graph Algorithm Based on Angular Distance Matching Score Transfer. *IEEE Sens. J.* **2024**, *24*, 6539–6547. [CrossRef]
22. Zhao, B.; Zhang, Y.; Yang, D.; Ren, T.; Yang, S.; Zhang, J.; Yang, J.; Sun, J.; Meng, X.; Yun, Z.; et al. Multidimensional Optimization-Improved Grid Star Map Recognition Algorithm. *Opt. Express* **2024**, *32*, 44280–44300. [CrossRef]
23. Dai, Y.; Shi, C.; Ben, L.; Zhu, H.; Zhang, R.; Wu, S.; Shan, S.; Xu, Y.; Zhou, W. Star Identification Algorithm Based on Dynamic Distance Ratio Matching. *Remote Sens.* **2025**, *17*, 62. [CrossRef]
24. Sun, Q.; Niu, Z.; Li, Y.; Wang, Z. A Robust High-Accuracy Star Map Matching Algorithm for Dense Star Scenes. *Remote Sens.* **2024**, *16*, 2035. [CrossRef]

25. Vallenari, A.; Brown, A.G.; Prusti, T.; De Bruijne, J.H.; Arenou, F.; Babusiaux, C.; Biermann, M.; Creevey, O.L.; Ducourant, C.; Evans, D.W.; et al. Gaia Data Release 3: Summary of the content and survey properties. *Astron. Astrophys.* **2023**, *674*, A1. [CrossRef]
26. Mortari, D.; Samaan, M.A.; Bruccoleri, C.; Junkins, J.L. The Pyramid Star Identification Technique. *Navigation* **2004**, *51*, 171–183. [CrossRef]
27. Kolomenkin, M.; Pollak, S.; Shimshoni, I.; Lindenbaum, M. Geometric voting algorithm for star trackers. *IEEE Trans. Aerosp. Electron. Syst.* **2008**, *44*, 441–456. [CrossRef]
28. Li, J.; Wei, X.G.; Zhang, G.J. Iterative algorithm for autonomous star identification. *IEEE Trans. Aerosp. Electron. Syst.* **2015**, *51*, 536. [CrossRef]